AJNR

Medical Imaging Compatibility of Magnesium- and Iron-Based Bioresorbable Flow Diverters

A.A. Oliver, E.K. Koons, P.S. Trester, J.E. Kleinow, R.S. Jonsgaard, A.J. Vercnocke, C. Bilgin, R. Kadirvel, S. Leng, A. Lu, D. Dragomir-Daescu and D.F. Kallmes

AJNR Am J Neuroradiol 2023, 44 (6) 668-674
doi: https://doi.org/10.3174/ajnr.A7873
http://www.ajnr.org/content/44/6/668

Medical Imaging Compatibility of Magnesium- and Iron-Based Bioresorbable Flow Diverters

A.A. Oliver, E.K. Koons, P.S. Trester, J.E. Kleinow, R.S. Jonsgaard, A.J. Vercnocke, C. Bilgin, R. Kadirvel, S. Leng, A. Lu, D. Dragomir-Daescu, and D.F. Kallmes

ABSTRACT

BACKGROUND AND PURPOSE: Bioresorbable flow diverters are under development to mitigate complications associated with conventional flow-diverter technology. One proposed advantage is the ability to reduce metal-induced artifacts in follow-up medical imaging. In the current work, the medical imaging compatibility of magnesium- and iron-based bioresorbable flow diverters is assessed relative to an FDA-approved control in phantom models.

MATERIALS AND METHODS: Bioresorbable flow diverters, primarily composed of braided magnesium or antiferromagnetic iron alloy wires, were compared with an FDA-approved control flow diverter. The devices were assessed for MR imaging safety in terms of magnetically induced force and radiofrequency heating using 1.5T, 3T, and 7T field strength clinical scanners. The devices were deployed in phantom models, and metal-induced image artifacts were assessed in the 3 MR imaging scanners and a clinical CT scanner following clinical scan protocols; device visibility was assessed under fluoroscopy.

RESULTS: The magnesium-based bioresorbable flow diverter, iron-based bioresorbable flow diverter, and the control device all demonstrated MR imaging safety in terms of magnetically induced force and radiofrequency heating at all 3 field strengths. The bioresorbable flow diverters did not elicit excessive MR imaging artifacts at any field strength relative to the control. Furthermore, the bioresorbable flow diverters appeared to reduce blooming artifacts in CT relative to the control. The iron-based bioresorbable flow diverter and control device were visible under standard fluoroscopy.

CONCLUSIONS: We have demonstrated the baseline medical imaging compatibility of magnesium and antiferromagnetic iron alloy bioresorbable flow diverters. Future work will evaluate the medical imaging characteristics of the bioresorbable flow diverters in large-animal models.

ABBREVIATIONS: BRFD = bioresorbable flow diverter; FD = flow-diverting device; FeBRFD = iron-based bioresorbable flow diverter; MgBRFD = magnesium-based bioresorbable flow diverter; RF = radiofrequency; T_g = gravitational torque; T_{max} = maximum torque

An estimated 5% of the US population has an intracranial aneurysm. Approximately 30,000 rupture annually, resulting in the death of one-half the patients within 6 months.[1] Therefore, it is critical to treat intracranial aneurysms before their rupture. Flow-diverting devices (FDs) are a rapidly growing endovascular approach for the treatment of intracranial aneurysms due to their high aneurysm occlusion rates in the clinic.[2] However, all FDA-approved FDs are composed of permanent materials that will remain in the patients for the duration of their lives. This outcome exacerbates complications such as device-induced thromboembolism[3,4] and stenosis of the parent artery.[5-7] Another limitation of FDs is metal-induced imaging artifacts.[8] These artifacts impede noninvasive follow-up CT and MR imaging of FD performance.[9] Metal-induced artifacts can obstruct the radiologist's view of tissues adjacent to the device, making it difficult to assess aneurysm healing, the degree of stenosis, and the presence of thrombi.

Bioresorbable flow diverters (BRFDs) are emerging as the next generation of FD technology to mitigate these complications.[10] BRFDs aim to serve their transient function of healing and occluding the aneurysm and subsequently to be safely resorbed into the body. BRFDs show promise in reducing metal-induced image

Received February 24, 2023; accepted after revision April 16.

From the Department of Biomedical Engineering and Physiology (A.A.O., E.K.K., S.L., D.D.-D., D.F.K.), Mayo Clinic Graduate School of Biomedical Sciences, Rochester, Minnesota; and Departments of Radiology (A.A.O., E.K.K., P.S.T., J.E.K., R.S.J., A.J.V., C.B., R.K., S.L., A.L., D.F.K.), Physiology and Biomedical Engineering (A.A.O., D.D.-D.), and Neurosurgery (R.K.), Mayo Clinic, Rochester, Minnesota.

This work was partially funded by National Institutes of Health, grant No. R01 NS076491. Alexander Oliver is supported by American Heart Association, grant No. 23PRE1012781.

Please address correspondence to Alexander A. Oliver, Alfred 9-446, Radiology, 200 First St SW, Mayo Clinic, Rochester, MN 55905; e-mail: Oliver.Alexander@mayo.edu

http://dx.doi.org/10.3174/ajnr.A7873

artifacts for 2 reasons: First, before any resorption, the innate material properties of many bioresorbable materials induce fewer metal artifacts than conventional FD materials.[11-13] Second, the progressive and eventual complete resorption reduces device volume and, therefore, metal-induced artifacts with time.[14]

We have previously developed BRFDs out of magnesium (MgBRFD) and iron (FeBRFD) alloys.[15] In the current work, we evaluate the medical imaging compatibility of the MgBRFD and FeBRFD relative to an FDA-approved control FD. MR imaging safety and both MR imaging and CT artifacts induced by the devices are assessed using phantom models. Device visibility for fluoroscopy-guided delivery is assessed using the same phantom models. This work serves as a baseline demonstration of the medical imaging compatibility of metallic bioresorbable vascular devices.

MATERIALS AND METHODS

Devices

The MgBRFDs and FeBRFDs have been previously described in detail.[15] In short, the MgBRFDs and FeBRFDs contained 32 and 48 braided wires, respectively. Three-quarters of the wires in each device are composed of bioresorbable magnesium (50-μm diameter) or iron (25-μm diameter) alloys. The iron alloy is composed of an austenitic crystal structure, theoretically resulting in antiferromagnetic properties.[16-18] The remaining wires are tantalum (30-μm diameter) to provide radiopacity during device delivery in vivo. The MgBRFDs and FeBRFDs were 4.75 mm in diameter and 10 mm in length. Wire subcomponents for both BRFDs were manufactured by Fort Wayne Metals. The Pipeline Embolization Device (Chestnut Medical) was used as the FDA-approved control FD. The control FD was composed of a braid of 36 cobalt chromium alloy and 12 platinum-tungsten wires (25- to 32-μm diameter). The control FD was 3.75 mm in diameter and 10 mm in length.

MR Imaging Evaluations

Magnetically Induced Force and Torque. The force induced on the devices by the magnetic field of clinical MR imaging scanners was evaluated with reference to ASTM F 2052–15 (ASNI Webstore).[19] The devices were hung from a stand using a string of negligible mass. The stand started at a position 90 cm away from the bore opening to the MR imaging scanner. The stand was then advanced toward the bore opening in 10 increments until it was 13 cm within the bore. Advancing the stand further within the bore obstructed the view of the device and made it impossible to assess the deflection angle. At every increment, the deflection angle was assessed using a protractor attached to the stand, as previously described.[14] Deflection angle estimations were rounded up to the nearest 5° increment to conservatively assess the magnetically induced force. Magnetically induced force, F_m, was calculated using the equation: $F_m = m \times g \times \tan(\alpha)$, where m is the mass of the device, g is the acceleration of gravity, and α is the deflection angle.[14] This process was repeated for the MgBRFD, FeBRFD, and control FD using 1.5T (Signa HDxt; GE Healthcare), 3T (Signa Premier; GE Healthcare), and 7T (Magnetom Terra; Siemens) clinical MR imaging scanners. The maximum spatial gradient within our area of measurement was 320, 550, and 500 G/cm for the 1.5T, 3T, and 7T scanners, respectively.

Magnetically induced torque on the implant was calculated using magnetically induced force in accordance with ASTM F2213 (ANSI Webstore).[20] The maximum torque (T_{max}) was estimated using the equation: $T_{max} = (B_{sat} \times F_m) / (4 \times dB/dz)$, where B_{sat} is the magnetic saturation of the device material, F_m is the magnetically induced force described above, and dB/dz is the maximum spatial gradient within our area of measurement. The B_{sat} of the device materials was unknown and was, therefore, conservatively estimated at 2.2T, the value for pure iron. Maximum gravitational torque (T_g) was calculated by multiplying the force of gravity acting on the device length.

Radiofrequency Heating. Radiofrequency (RF)-induced heating of the devices was evaluated with reference to ASTM F 2182–1121 (ASTM). An MgBRFD, FeBRFD, or control FD was placed in a phantom composed of 1.32 g/L of NaCl and 10 g/L of polyacrylic acid in deionized water to simulate physiologic electrical and thermal properties.[21] Two temperature probes were placed on the surface of the device, with one in the middle and one at the end of the device. The device was held in place in the phantom using a wooden dowel. A third temperature probe was placed in the phantom far from the device to measure background fluctuations in phantom temperature. The phantom and the device were placed as laterally as possible on the patient table where potential RF heating is expected to be worse than in the center of the bore. Each device type or phantom was imaged using a T1-weighted fast spin-echo sequence on the 1.5T, 3.T, and 7T clinical MR imaging scanners. Specific scan parameters are presented in the Online Supplemental Data. Temperature was measured for 2 minutes before the scan and for the duration of the scan sequence. For each temperature probe, the difference in average temperature between the prescan and scan duration was calculated. The temperature changes from the 2 probes at the device surface were averaged together, and the temperature change from the background probe was subtracted from this average.

Imaging Artifacts. An MgBRFD, FeBRFD, or control FD was placed within the phantom described above and imaged with a T1-weighted fast spin-echo sequence and a gradient-echo sequence using the 1.5 T, 3T, and 7T clinical MR imaging scanners. The specific scan parameters for both sequences are presented in the Online Supplemental Data. All scans were completed in first level operating mode.

CT Artifacts. An MgBRFD, FeBRFD, or a control FD was deployed within silicone sidewall aneurysm models. The aneurysm neck was 4 mm, and the height and width were 8 mm. The parent artery diameter was 4 mm for the MgBRFD and FeBRFD and 3.75 mm for the control FD to appropriately match the device diameters. The devices containing aneurysm models were perfused with Omnipaque iodine contrast (GE Healthcare) diluted to a concentration of 20 mg/mL using deionized water and placed within a 20-cm water phantom to mimic contrast-enhanced neurovasculature and attenuation in the human head. The samples were scanned using a clinical energy-integrating detector CT scanner (Somatom Force; Siemens) following the dual-source, dual-energy clinical circle of Willis protocol at our institution. The scan parameters are presented in the Online

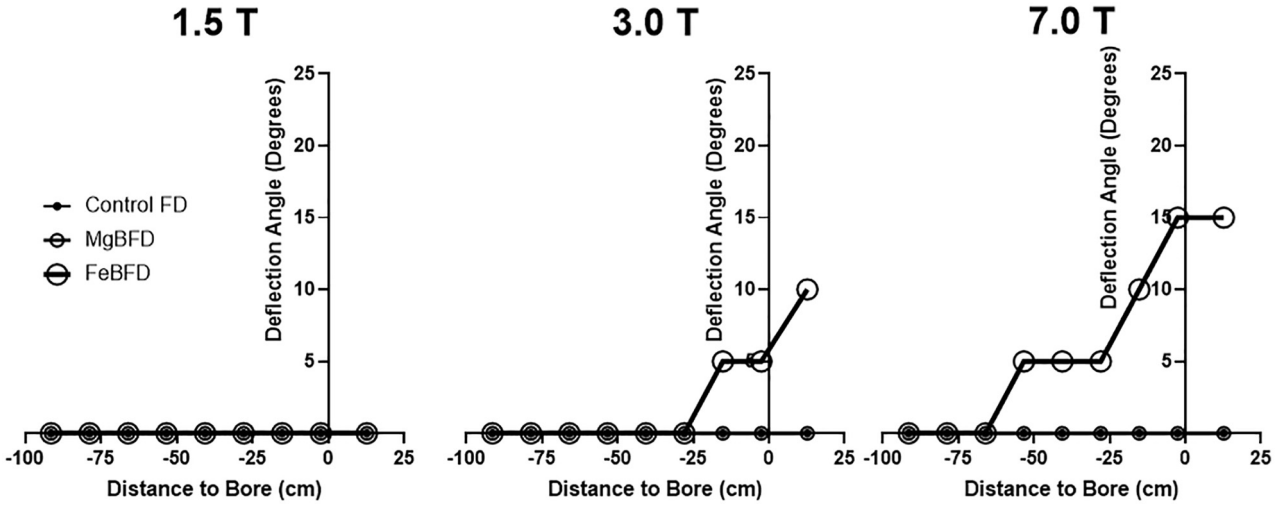

FIG 1. Deflection angle of the control FD, MgBRFD, and FeBRFD at various locations relative to the bore opening of 1.5T, 3T, and 7T field strength clinical MR imaging scanners. Negative values are outside the bore, with 0 cm representing the bore opening. Deflection angle estimates are rounded up to the next highest 5° increment.

Supplemental Data. The first scan before any device resorption was considered the 0-week time point.

The models containing MgBRFDs and FeBRFDs were then incorporated into a flow loop mimicking the physiologic environment to simulate device resorption using methods previously described in detail.[15] At 1-, 5-, and 12-week time points, the devices were removed from the flow loop and imaged using a micro-CT scanner (SkyScan 1276; Bruker) to quantify reductions in device volume across time, as previously described.[15] Immediately following micro-CT imaging, the device-containing models were perfused with contrast and re-imaged with the clinical CT scanner using the same technique as the 0-week time point. Following each scan, the device-containing models were re-incorporated into the flow loop until the next scan. This step allowed us to investigate changes in clinical CT artifacts associated with device resorption with time.

Fluoroscopy. A MgBRFD, FeBRFD, and control FD were deployed within the same silicone aneurysm models and placed within the 20-cm water phantom described above. The devices were then imaged using an Artis Zee angiography unit (Siemens) to assess their visibility for fluoroscopy-guided delivery. The devices containing the silicone aneurysm models were then removed from the 20-cm water phantom and imaged directly on the tabletop to more clearly depict the devices. The same x-ray tube position and angle were used for the water phantom and tabletop tests. The distance of the x-ray tube to aneurysm models was also standardized.

RESULTS

Magnetically Induced Force, Torque, and RF Heating

The deflection angles of the control FD, MgBRFD, and FeBRFD at various locations relative to the bore opening of 1.5T, 3T, and 7T clinical MR imaging scanners are presented in Fig 1. The magnetic fields of the MR imaging scanners did not induce any detectable deflection for the control FD and the MgBRFD at any field strength. The FeBRFD deflected 5° and 15° at the bore opening of the 3T and 7T strength scanners, respectively. The calculated force of gravity (F_g), magnetically induced force (F_m) at the bore opening, and the ratio F_m/F_g are presented in the Online Supplemental Data for all device types and field strength scanners. Although the FeBRFD experienced detectable deflection at the bore opening of the 3T and 7T scanners, the magnetically induced force acting on the device from the MR imaging scanner was less than one-third of the force of gravity acting on the device ($F_m/F_g = 0.09$ at 3T, $F_m/F_g = 0.27$ at 7T) in the area tested. Because the highest spatial gradient of the magnetic field is <3 times the maximum spatial gradient within the area of our measurements, the magnetically induced force, therefore, does not present a notable safety concern for the control FD, MgBRFD, and FeBRFD.

In theory, the austenitic crystal structure of the iron alloy used in FeBRFD should result in a completely nonferromagnetic device and consequently no magnetically induced force. The small observed deflections are likely due to tiny ferromagnetic impurities within the crystal structure of the iron alloy. The T_{max} on the devices was estimated using F_m, T_{max}, and T_g, and the ratio of T_{max}/T_g is presented in Online Supplemental Data for all device types and field strength scanners. No torque was estimated for the control FD and MgBRFD at any scanner strength. The estimated T_{max} of the FeBRFD was less than the gravitational torque in the 3T scanner, but approximately 3 times greater than T_g in the 7T scanner ($T_{max}/T_g = 0.8$ at 3T, $T_{max}/T_g = 2.8$ at 7T). These estimations indicate that the FeBRFD is MR imaging–conditional at 3T, and further considerations would be required for evaluating safety at 7T. However, our T_{max} estimations are likely overestimates, because the B_{sat} for the antiferromagnetic resorbable iron alloy is likely much less than the 2.2T value conservatively used on the basis of pure iron.

For the evaluation of RF heating, no device type at any field strength resulted in a change in temperature of >0.34°C. The small observed RF heating temperature changes are within the range of fluctuations in room temperature and are negligible

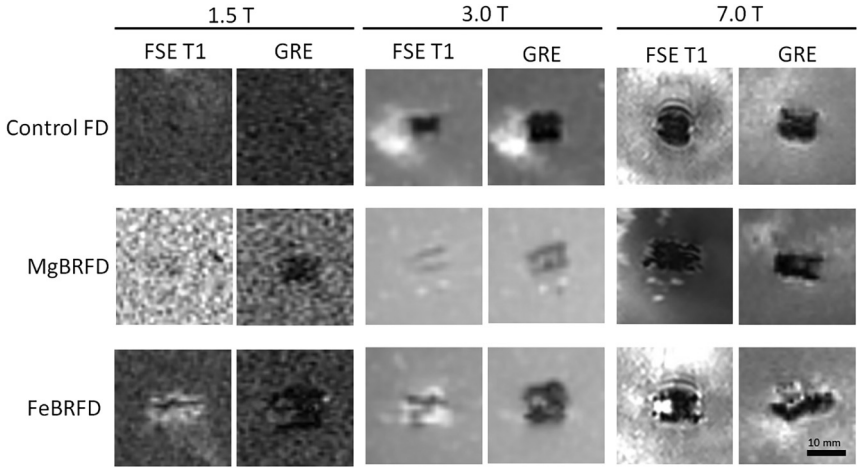

FIG 2. MR imaging artifacts induced by the control FD, MgBRFD, and FeBRFD using a fast spin-echo sequence with T1 weighting (FSE T1) and a gradient recalled-echo (GRE) scan sequence with 1.5T, 3T, and 7T field strength clinical MR imaging scanners.

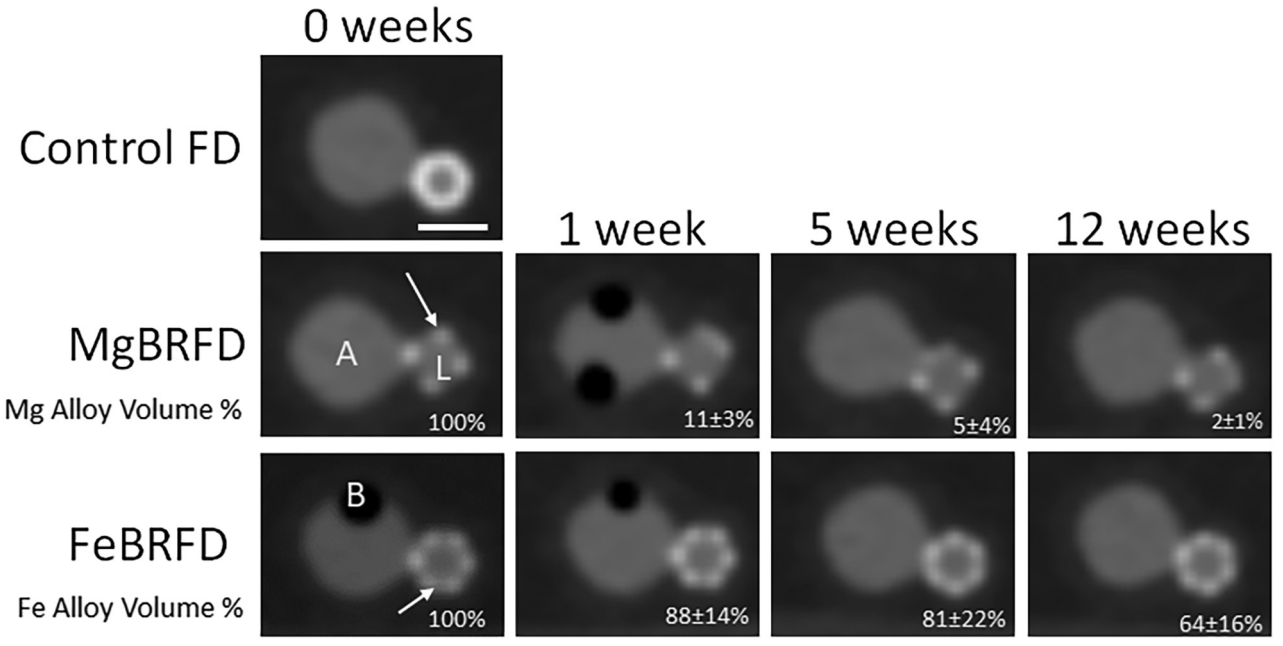

FIG 3. Representative CT images of the control FD, MgBRFD, and FeBRFD and reduction in resorbable device volume with time. A represents the aneurysm sac, L represents the lumen of the parent artery, and B represents trapped air bubbles. The *arrows* indicate examples of crossing tantalum marker wires. The scale bar is 5 mm.

from a physiologic safety standpoint. Therefore, these data suggest that the control FD, MgBRFD, and FeBRFD are MR imaging–conditional and can be safely scanned at the tested field strengths from the RF heating perspective.

MR Imaging Artifacts

MR imaging artifacts from the control FD, MgBRFD, and FeBRFD using both a T1-weighted fast spin-echo sequence and a gradient-echo scan sequence for all 3 field strength MR imaging scanners are presented in Fig 2. The MgBRFD imaged with the fast spin-echo sequence and the control FD for both scan sequences are barely detectable at 1.5T. Generally, for each device type, the gradient-echo sequence induced larger artifacts than the fast spin-echo sequence. However, the actual size of the artifacts depends on many acquisition parameters such as TE, echo-train length, acquisition bandwidth, the orientation of the device in the scanner bore, and so forth. The FeBRFD appeared to induce slightly more artifacts than the control FD and MgBRFD when matched for scan sequence and scanner strength. Overall, MR imaging artifacts induced by the MgBRFD and FeBRFD are not excessive relative to the control FD, suggesting suitable MR imaging compatibility for the bioresorbable devices.

CT Artifacts

Representative CT images of the control FD, MgBRFD, and FeBRFD, as well as reductions in resorbable material volume are presented in Fig 3. The control FD induced the most blooming artifacts, resulting in the device appearing larger than its physical

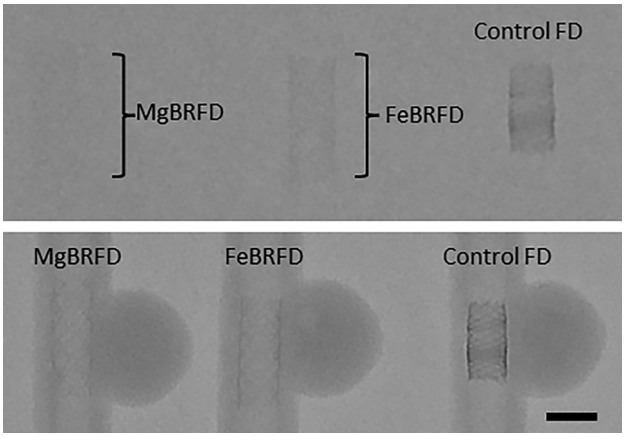

FIG 4. Fluoroscopic images of the MgBRFD, FeBRFD, and control FD placed within a 20-cm water phantom (*top*) and directly onto the tabletop (*bottom*). The scale bar is 5 mm.

size. No struts were visible in the control FD, making it appear as a solid cylinder due to blooming artifacts of highly attenuating metals. This feature obstructed the view of the aneurysm neck and made the parent vessel appear more stenosed. For the MgBRFD and FeBRFD, the only apparent struts were the tantalum radiopaque marker wires. Representative images for the MgBRFDs and FeBRFDs were selected at locations where the tantalum wires within the braid crossed, making it appear as if there were half the amount of tantalum wires than physically present. These locations were selected to create larger regions of bioresorbable wires unimpeded by the blooming of adjacent tantalum wires. The magnesium alloy resorbable wires were not detected at 0 weeks because their CT numbers were very similar to the contrast within the aneurysm model. Consequently, their resorption with time and near-complete resorption at 5 weeks did not have any visible implications for image quality. It is difficult to discern whether the iron alloy resorbable wires are detectable between the tantalum struts or if the increased CT number relative to the contrast is caused by blooming of the adjacent tantalum wires. A reduction down to 65% of the initial bioresorbable iron alloy volume as determined by micro-CT at 12 weeks did not appear to influence the resulting images.

Fluoroscopy

Fluoroscopy images of the MgBRFD, FeBRFD, and the control FD are presented in Fig 4. When placed in the 20-cm water phantom (FOV = 32 cm, kV = 70, mA = 258), the MgBRFD is barely detectable. The FeBRFD is more visible, owing to the greater number of tantalum wires within the braid in addition to the higher density of the iron alloy over the magnesium alloy. The control FD is the most apparent. When removed from the water phantom, all 3 devices are detectable, and the braided structure becomes more visible (FOV = 32 cm, kV = 70, mA = 31). Our incorporation of twelve 30-μm-diameter tantalum wires in the FeBRFD resulted in an overall device radiopacity that would likely be suitable for fluoroscopy-guided delivery. However, these images also suggest that the device design could be improved in this respect. The ideal FD design requires a balance between fluoroscopic visibility and minimal CT artifacts.

DISCUSSION

In the current work, we demonstrate the medical imaging compatibility of a novel MgBRFD and FeBRFD relative to an FDA-approved control FD. With reference to the FDA guidance document "Testing and Labeling Medical Devices for Safety in the Magnetic Resonance Environment,"[22] all 3 devices were MR imaging–conditional from a magnetically induced force and RF heating standpoint at all MR imaging scanner strengths. The FDA suggests that passive devices such as FDs $<$2 cm in all dimensions and $<$3 cm away from other implants do not require RF heating evaluations at $\leq$3T, because they are not expected to generate a temperature change of $>$2°C.[22] Our results validate this point and expand it up to a 7T scanner. The magnetically induced torque of all 3 devices was less than the T_g in all 3 scanners, other than the FeBRFD in the 7T scanner. Devices with a lower magnetically induced torque than T_g are considered MR imaging conditional.[22] However, a greater magnetically induced torque may still be acceptable depending on the type of tissue adjacent to the device and how the device is fastened within it.[22] In the case of stents and FDs, it may be necessary to wait several months until the device is encapsulated by tissue before obtaining MR images. Finally, the MgBRFD and FeBRFD did not induce excessive MR imaging artifacts relative to the control FD.

The MgBRFD and FeBRFD appeared to reduce blooming artifacts in CT images relative to the control FD, and the FeBRFD was still visible under fluoroscopy. This feature may result in a more accurate assessment of healing at the aneurysm neck and device-induced stenosis in follow-up imaging. The only obvious CT artifacts in the MgBRFD and FeBRFD images were caused by the tantalum marker wires. This feature suggests that an optimal BRFD design should contain the minimum volume of radiopaque markers required for fluoroscopy-guided delivery, while maximizing the amount of resorbable magnesium or iron alloy components within the device. Magnesium and iron alloys are regularly applied to other vascular scaffolding applications, such as coronary stenting.[23] This work can also serve as a baseline demonstration of medical imaging compatibility for these devices.

Other groups have investigated the medical imaging compatibility of BRFDs. Morrish et al[11] demonstrated suitable visibility for fluoroscopy-guided device delivery of their primarily polymer-based BRFD. Furthermore, they demonstrated a quantitative reduction in device-induced artifacts in MR imaging and CT images when their BRFD was compared with an FDA-approved control FD. They also showed that their BRFDs improved the image quality of MR imaging when assessed by 8 blinded neuroradiologists. Their work showcased the ability of BRFDs to reduce device-induced artifacts and improve medical imaging quality. Our work investigates and extends these results to the imaging compatibility of metallic BRFDs. Bian et al[14] investigated the MR imaging compatibility of a bioresorbable iron–based coronary stent. Their stent was primarily composed of a ferromagnetic nitrided iron backbone. The ferromagnetic properties resulted in magnetically induced forces from the MR imaging scanners that were substantially larger than the force of gravity acting on the devices. However, RF heating and image artifacts were negligible relative to industry-standard controls. Most notably, their devices demonstrated the ability to reduce artifacts with their progressive resorption across time in vivo.

DSA is currently the criterion standard follow-up technique because its quality is not affected by device-related metallic artifacts.[24] However, DSA is an invasive procedure with potential complications that include cerebral microembolism and puncture site hematoma and pseudoaneurysm.[24] Therefore, there has been growing interest in the use of noninvasive techniques such as CT and MR imaging in the follow-up of aneurysms treated by endovascular means. The current literature indicates that noninvasive imaging methods are safer and more cost-effective compared with DSA as a primary follow-up technique.[25,26] However, CT and MR imaging are susceptible to metal artifacts, which can affect the quality of scan and assessment. Vascular device design and material selection have implications for CT and MR imaging compatibility.[9,27,28] Halitcan et al[8] recently reported that nitinol FDs are advantageous for clinical TOF MR angiography follow-up of FD performance over cobalt-chromium FDs. In CT imaging, both the strut thickness and material selection affect the degree of x-ray attenuation and consequently the extent of metal-induced artifacts.[29,30] Additionally, the improvement of medical imaging technology to mitigate metal-induced image artifacts and enhance the image quality of endovascular devices remains a growing topic of research.[31,32] Follow-up quality assessment of medical imaging should be considered in the development and engineering of endovascular devices.

A limitation of the study was that the available control FD was 1 mm smaller in diameter than the MgBRFD and FeBRFD. However, the slightly decreased metal volume and dimensions in the control FD acted as a slightly more conservative benchmark standard for the BRFDs. Another limitation was the accuracy of deflection angle measurements, which were assessed visually relative to a mounted adjacent protractor. However, all observed deflection angles at multiple distances to the bore at all 3 field strengths and resulting calculations of magnetically induced force were less than one-third of the force of gravity acting on the devices; therefore, all measurement errors were negligible in the overall assessment of MR imaging safety.

Future work will focus on assessing the long-term aneurysm occlusion rates of the bioresorbable FDs relative to permanent controls in the rabbit elastase–induced aneurysm model.[33] A major direction for the field is to determine the optimal device resorption rate that allows the device to maintain structural integrity long enough for the aneurysm to heal before notable resorption.[10] The medical imaging characteristics of the MgBRFD and FeBRFD relative to a control FD will also be assessed using animal models. Blinded interventional neuroradiologists will assess the deployability and image quality of the MgBRFDs and FeBRFDs relative to the control FDs using Likert scales. Future work will also focus on improving the MgBRFD and FeBRFD design by reducing the amount of radiopaque marker wires within the braid and/or adding platinum pledgets on either end of the device, with the intention of minimizing image artifacts at the aneurysm neck without sacrificing deployability.

CONCLUSIONS

We have demonstrated the MR imaging compatibility of magnesium- and antiferromagnetic iron alloy–based BRFDs. Furthermore, the BRFDs appeared to reduce metal-induced CT blooming artifacts relative to the FDA-approved control FD. These data suggest that minimizing the volume of radiopaque markers required for fluoroscopy-guided device delivery, while maximizing the amount of bioresorbable metal components in the device, could reduce CT artifacts. This work serves as a baseline demonstration of the medical imaging compatibility of bioresorbable magnesium and antiferromagnetic iron alloy vascular devices. Future work will investigate the medical imaging characteristics of the BRFDs using large-animal models.

ACKNOWLEDGMENTS

The authors would like to thank Jeffrey Marsh, Liqiang Ren, and Tim Winfree for their help with CT scan acquisitions and Dr Daying Dai for her help formatting figures.

Disclosure forms provided by the authors are available with the full text and PDF of this article at www.ajnr.org.

REFERENCES

1. King JT Jr. **Epidemiology of aneurysmal subarachnoid hemorrhage.** *Neuroimaging Clin N Am* 1997;7:659–68 Medline
2. Brinjikji W, Murad MH, Lanzino G, et al. **Endovascular treatment of intracranial aneurysms with flow diverters: a meta-analysis.** *Stroke* 2013;44:442–47 CrossRef Medline
3. Kallmes DF, Hanel R, Lopes D, et al. **International retrospective study of the Pipeline embolization device: a multicenter aneurysm treatment study.** *AJNR Am J Neuroradiol* 2015;36:108–15 CrossRef Medline
4. Becske T, Brinjikji W, Potts MB, et al. **Long-term clinical and angiographic outcomes following Pipeline embolization device treatment of complex internal carotid artery aneurysms: five-year results of the Pipeline for Uncoilable or Failed Aneurysms Trial.** *Neurosurgery* 2017;80:40–48 CrossRef Medline
5. Guédon A, Clarençon F, Di Maria F, et al. **Very late ischemic complications in flow-diverter stents: a retrospective analysis of a single-center series**. *J Neurosurg* 2016;125:929–35 CrossRef Medline
6. Caroff J, Tamura T, King RM, et al. **Phosphorylcholine surface modified flow diverter associated with reduced intimal hyperplasia.** *J Neurointerv Surg* 2018;10:1097–101 CrossRef Medline
7. Flood TF, van der Bom IM, Strittmatter L, et al. **Quantitative analysis of high-resolution, contrast-enhanced, cone-beam CT for the detection of intracranial in-stent hyperplasia.** *J Neurointerv Surg* 2015;7:118–25 CrossRef Medline
8. Halitcan B, Bige S, Sinan B, et al. **The implications of magnetic resonance angiography artifacts caused by different types of intracranial flow diverters.** *J Cardiovasc Magn Reson* 2021;23:1–14 CrossRef Medline
9. Bouillot P, Brina O, Delattre BM, et al. **Neurovascular stent artifacts in 3D-TOF and 3D-PCMRI: influence of stent design on flow measurement**. *Magn Reson Med* 2019;81:560–72 CrossRef Medline
10. Oliver AA, Carlson KD, Bilgin C, et al. **Bioresorbable flow diverters for the treatment of intracranial aneurysms: review of current literature and future directions.** *J Neurointerv Surg* 2023;15:178–82 CrossRef
11. Morrish R, Corcoran R, Cooke J, et al. **Fluoroscopy, CT, and MR imaging characteristics of a novel primarily bioresorbable flow-diverting stent for aneurysms.** *Interv Neuroradiol* 2022;28:660–67 CrossRef Medline
12. Filli L, Luechinger R, Frauenfelder T, et al. **Metal-induced artifacts in computed tomography and magnetic resonance imaging: comparison of a biodegradable magnesium alloy versus titanium and stainless steel controls.** *Skeletal Radiol* 2015;44:849–56 CrossRef Medline
13. Sonnow L, Könneker S, Vogt PM, et al. **Biodegradable magnesium Herbert screw: image quality and artifacts with radiography, CT and MRI**. *BMC Med Imaging* 2017;17:1–9 CrossRef Medline

14. Bian D, Qin L, Lin W, et al. **Magnetic resonance (MR) safety and compatibility of a novel iron bioresorbable scaffold.** *Bioact Mater* 2020;5:260–74 CrossRef Medline
15. Oliver AA, Bilgin C, Vercnocke AJ, et al. **Benchtop proof of concept and comparison of iron and magnesium-based bioresorbable flow diverters.** *J Neurosurg* 2022;1:1–7 CrossRef Medline
16. Schaffer JE, Nauman EA, Stanciu LA. **Cold-drawn bioabsorbable ferrous and ferrous composite wires: an evaluation of mechanical strength and fatigue durability.** *Metallurgical and Materials Transactions B* 2012;43:984–94 CrossRef
17. Schaffer JE. **Biodegradable alloy wire for medical devices.** *Google Patents* 2020. https://patents.google.com/patent/WO2014011803A1/en. Accessed April 29, 2023
18. Ishikawa Y, Endoh Y. **Antiferromagnetism of γ-FeMn alloys**. *J Appl Phys* 1968;39:1318–19 CrossRef
19. ASTM A. **F2052-15: Standard Test Method for Measurement of Magnetically Induced Displacement Force on Medical Devices in the Magnetic Resonance Environment**. *ANSI Webstore*. 2015. https://webstore.ansi.org/standards/astm/astmf205215. Accessed April 29, 2023
20. ASTM IF2213-17. **Standard Test Method for Measurement of Magnetically Induced Torque on Medical Devices in the Magnetic Resonance Environment.** *ASTM Compass* 2017. https://www.astm.org/f2213-17.html. Accessed April 29, 2023
21. ASTM F2182-11a. **Standard Test Method for Measurement of Radio Frequency Induced Heating on or Near Passive Implants during Magnetic Resonance Imaging.** *ASTM International West* 2011. https://webstore.ansi.org/standards/astm/astmf218211a. Accessed April 29, 2023
22. US Food and Drug Administration. **Testing and labeling medical devices for safety in the magnetic resonance (MR) environment: Guidance for industry and Food and Drug Administration Staff.** *Federal Register* 2021
23. Oliver AA, Sikora-Jasinska M, Demir AG, et al. **Recent advances and directions in the development of bioresorbable metallic cardiovascular stents: insights from recent human and in vivo studies.** *Acta Biomater* 2021;127:1–23 CrossRef Medline
24. Soize S, Gawlitza M, Raoult H, et al. **Imaging follow-up of intracranial aneurysms treated by endovascular means: why, when, and how?** *Stroke* 2016;47:1407–12 CrossRef Medline
25. Schaafsma JD, Koffijberg H, Buskens E, et al. **Cost-effectiveness of magnetic resonance angiography versus intra-arterial digital subtraction angiography to follow-up patients with coiled intracranial aneurysms.** *Stroke* 2010;41:1736–42 CrossRef Medline
26. Burel J, Gerardin E, Vannier M, et al. **Follow-up of intracranial aneurysms treated by flow diverters: evaluation of parent artery patency using 3D-T1 gradient recalled-echo imaging with 2-point Dixon in combination with 3D-TOF-MRA with compressed sensing.** *AJNR Am J Neuroradiol* 2022;43:554–59 CrossRef Medline
27. Lenhart M, Völk M, Manke C, et al. **Stent appearance at contrast-enhanced MR angiography: in vitro examination with 14 stents**. *Radiology* 2000;217:173–78 CrossRef Medline
28. Mahnken AH. **CT imaging of coronary stents: past, present, and future.** *ISRN Cardiol* 2012;2012:1–12 CrossRef Medline
29. Mahnken AH, Buecker A, Wildberger JE, et al. **Coronary artery stents in multislice computed tomography: in vitro artifact evaluation.** *Invest Radiol* 2004;39:27–33 CrossRef Medline
30. Maintz D, Burg MC, Seifarth H, et al. **Update on multidetector coronary CT angiography of coronary stents: in vitro evaluation of 29 different stent types with dual-source CT.** *Eur Radiol* 2009;19:42–49 CrossRef Medline
31. Leng S, Bruesewitz M, Tao S, et al. **Photon-counting detector CT: system design and clinical applications of an emerging technology.** *Radiographics* 2019;39:729–43 CrossRef Medline
32. Lee EM, Ibrahim E-SH, Dudek N, et al. **Improving MR image quality in patients with metallic implants.** *Radiographics* 2021;41:E126–37 CrossRef Medline
33. Fujiwara NH, Cloft HJ, Marx WF, et al. **Serial angiography in an elastase-induced aneurysm model in rabbits: evidence for progressive aneurysm enlargement after creation.** *AJNR Am J Neuroradiol* 2001;22:698–703 Medline